Research Square

Preprints are preliminary reports that have not undergone peer review.
They should not be considered conclusive, used to inform clinical practice,
or referenced by the media as validated information.

Endothelial Injury Associated with PFOA and PFOS Exposure: Insights from Network Toxicology and Experimental Validation

liu honghui
Anhui University of Science and Technology
Chenyan Wang
Zhongnan Hospital of Wuhan University
Dong Chen
School of Public Health, Anhui University of Science and Technolog
Qiqi Dong
School of Public Health, Anhui University of Science and Technolog
Yan Wang
Southeast University
Chao Lu
Chaolu@aust.edu.cn

The First Affiliated Hospital of Anhui University of Science and Technology (Huainan First People's Hospital)

Research Article

Keywords: perfluorooctanoic acid, perfluorooctane sulfonate, network toxicology, endothelial dysfunction, c-Jun, p53

Posted Date: November 20th, 2026

DOI: https://doi.org/10.21203/rs.3.rs-11605715/v1

License: This work is licensed under a Creative Commons Attribution 4.0 International License.
Read Full License

Additional Declarations: No competing interests reported.

Endothelial Injury Associated with PFOA and PFOS Exposure: Insights from Network Toxicology and Experimental Validation

Honghui Liu[a]†, Chenyan Wang[d]†, Dong Chen[b]†, Qiqi Dong[b]*, Yan Wang[e]*, Chao Lu[c]*

[a] School of Safety Science and Engineering, Anhui University of Science and Technology, Huainan 232001, Anhui, China

[b] School of Public Health, Anhui University of Science and Technology, Hefei 231131, Anhui, China

[c] The First Affiliated Hospital of Anhui University of Science and Technology (Huainan First People's Hospital), Huainan 232007, Anhui, China

[d] Department of Gastroenterology, Zhongnan Hospital of Wuhan University, Wuhan 430071, Hubei, China

[e] Department of Hematology, Zhongda Hospital, School of Medicine, Southeast University; Institute of Hematology, Southeast University, Nanjing 210009, Jiangsu, China

† These authors contributed equally to this work and share first authorship.

* Corresponding authors: Qiqi Dong (2345011009@stu.ahmu.edu.cn); Yan Wang (2257164901@qq.com); Chao Lu (Chaolu@aust.edu.cn).

Abstract

Background: Perfluorooctanoic acid (PFOA) and perfluorooctane sulfonate (PFOS) are persistent environmental contaminants that may affect vascular function. We combined network toxicology, molecular modeling, and human umbilical vein endothelial cell (HUVEC) assays to compare their predicted molecular interactions and short-term endothelial effects.

Results: Cross-referencing chemical-associated genes with six diabetic-complication gene sets identified JUN and TP53 as recurrent candidate nodes. Docking scores were similar, whereas 100-ns molecular dynamics and molecular mechanics Poisson–Boltzmann surface area (MM-PBSA) analyses showed lower whole-complex root mean square deviation (RMSD) and a more favorable estimated binding free energy for the PFOS–p53 model than for PFOA–p53. HUVECs were exposed to PFOA (50 μM), PFOS (50 μM), or their mixture (50 μM each). At 24 h, PFOS increased p-c-Jun/c-Jun and p-p65/p65 ratios, p53 and intercellular adhesion molecule 1 (ICAM-1) protein levels, and inflammatory gene expression, while reducing migration. All exposure conditions reduced junction numbers in a 12-h vascular-like network formation assay. The phosphorylated-to-total endothelial nitric oxide synthase (p-eNOS/eNOS) ratio was not significantly altered, and the mixture produced endpoint-dependent effects.

Conclusions: These results identify distinct short-term endothelial responses to PFOA and PFOS, with PFOS eliciting more pronounced inflammation-associated changes under the tested conditions.

Keywords: perfluorooctanoic acid; perfluorooctane sulfonate; network toxicology; endothelial dysfunction; c-Jun; p53

1. Background

Per- and polyfluoroalkyl substances (PFAS) are a class of highly persistent fluorinated chemicals widely used in industrial and consumer applications, including surface treatments and firefighting foams. Owing to the exceptional chemical stability of carbon–fluorine bonds, PFAS can persist in the environment and lead to continuous human exposure through drinking water, food, indoor environments, and occupational contact (Buck et al. 2012; De Silva et al. 2021; Glüge et al. 2020). Perfluorooctanoic acid (PFOA) and perfluorooctane sulfonate (PFOS) are among the most extensively studied legacy long-chain PFAS. Although their production and use have been restricted in many regions, they remain toxicologically relevant because of historical emissions, environmental persistence, and slow biological elimination (Sunderland et al. 2019). Growing evidence suggests that PFAS exposure may be associated with disturbances in glucose homeostasis, insulin signaling, and other metabolic and endocrine processes, although epidemiological associations with type 2 diabetes remain inconsistent across populations and exposure settings (Gui et al. 2023; Margolis and Sant 2021).

Vascular endothelial cells can respond to chemical insults through inflammatory signaling, redox imbalance and changes in repair-related functions. These processes are also relevant to diabetic vascular complications, which involve multiple organs and tissue types. Endothelial dysfunction is involved in the development of several diabetic complications, suggesting that common molecular pathways may contribute to vascular injury across different disease contexts (Schalkwijk and Stehouwer 2005; Shi and Vanhoutte 2017). Identifying molecular features associated with both PFAS exposure and diabetic complications may therefore provide insight into their potential biological connections.

Previous studies have shown that PFOS can induce oxidative stress in endothelial cells, alter endothelial permeability, promote inflammatory responses and adhesion-molecule expression, and affect vascular-like structure formation (Forsthuber et al. 2022; Liao et al. 2012; Qian et al. 2010). However, whether common PFAS-associated molecular nodes can be identified across different

diabetic complications remains unclear. Network toxicology provides a systematic approach for integrating chemical-associated targets with disease-related gene sets and identifying candidate genes and signaling pathways (Qi et al. 2026). Combining network analysis with molecular modeling and endothelial cell experiments may help characterize molecular and functional responses associated with PFAS exposure.

PFOA and PFOS are legacy long-chain PFAS that contain carboxylate and sulfonate head groups, respectively. These structural differences may influence their interactions with proteins and their biological effects. Comparing the two compounds may therefore help identify similarities and differences in their predicted molecular interactions and endothelial responses. In addition, examining their combined exposure may provide further information about the cellular responses associated with simultaneous exposure to these contaminants.

In this study, we integrated network toxicology, molecular modeling and human umbilical vein endothelial cell (HUVEC) experiments to compare the effects of PFOA, PFOS and their combined exposure. Genes associated with the two compounds were analyzed alongside gene sets from six diabetic complications to identify recurrent candidate molecular nodes. *JUN* and *TP53* were subsequently examined using molecular docking, 100-ns molecular dynamics (MD) simulations and molecular mechanics Poisson–Boltzmann surface area (MM-PBSA) analysis. The effects of PFOA, PFOS and their mixture on inflammatory and stress-related proteins, cytokine expression, cell migration and vascular-like network formation were then evaluated in HUVECs. This combined approach was used to compare the predicted molecular interactions and cellular responses associated with the two compounds.

2. Methods

2.1. Collection of PFOA/PFOS-associated targets

The molecular structures of PFOA and PFOS were obtained from PubChem (Compound IDs 9554 and 74483, respectively). Simplified molecular-input line-entry system (SMILES) strings and three-dimensional conformations were collected, and the deprotonated anionic forms were used for subsequent structural analyses. PFOA- and PFOS-associated genes and predicted protein targets were retrieved from the Comparative Toxicogenomics Database (CTD), SwissTargetPrediction, ChEMBL,

and the Similarity Ensemble Approach (SEA). *Homo sapiens* was selected as the target species for SwissTargetPrediction. Records from the other databases were retained when they could be unambiguously mapped to human genes or proteins. Identifiers were standardized to approved human gene symbols using UniProt, and duplicate or unmappable entries were removed. The resulting lists were defined as the PFOA- and PFOS-associated target sets, and their intersection was used for downstream disease-network analyses.

2.2. Collection of diabetic complication-associated genes

Genes associated with diabetic nephropathy, diabetic retinopathy, diabetic neuropathy, diabetic foot ulcer, diabetic vascular dysfunction, and diabetic cardiomyopathy were collected from GeneCards, Online Mendelian Inheritance in Man (OMIM), DrugBank, and the Therapeutic Target Database (TTD). GeneCards records with a relevance score ≥10 were retained. Records from the other databases were included when they could be clearly mapped to human genes. Gene symbols were standardized according to HUGO Gene Nomenclature Committee (HGNC) nomenclature, and duplicate or unmappable entries were removed. For each complication, the disease-associated gene set was intersected with the shared PFOA/PFOS target set.

2.3. Protein–protein interaction and hub-gene analysis

For each diabetic complication, the proteins encoded by the overlapping genes were used to construct protein–protein interaction (PPI) networks in STRING version 12.0, with *Homo sapiens* selected as the organism and the minimum required interaction score set to 0.900 (Szklarczyk et al. 2023). The resulting PPI networks were imported into Cytoscape version 3.10.1, and isolated nodes were removed. Network nodes were ranked using six algorithms implemented in the cytoHubba plugin: maximal clique centrality (MCC), Degree, Closeness, Radiality, Betweenness, and Stress (Chin et al. 2014). The top 10 nodes identified by each algorithm were retained. The corresponding genes appearing among the top 10 nodes of all six algorithms within a given disease network were defined as consensus hub genes, whereas genes meeting this criterion across all six disease networks were defined as cross-disease consensus hub genes.

2.4. Functional enrichment analysis

The complication-specific overlapping gene sets were analyzed separately using Metascape, with *Homo sapiens* selected as the species and all other parameters set to the platform defaults (Zhou et al. 2019). Gene Ontology (GO) analysis included biological process, cellular component, and molecular function categories, whereas Kyoto Encyclopedia of Genes and Genomes (KEGG) analysis was used to identify enriched pathways. Enrichment results were visualized in R using ggplot2. GO terms were ranked and colored according to adjusted P values, whereas KEGG pathways were ranked and colored according to P values.

2.5. Molecular docking

The c-Jun basic leucine zipper (bZIP) domain construct (PDB ID: 1JNM) and the human p53 DNA-binding core domain (PDB ID: 2OCJ) were obtained from the RCSB Protein Data Bank for molecular docking with PFOA and PFOS. Protein structures were prepared using PDBFixer. For 1JNM, the c-Jun dimer was retained and the bound DNA was removed; for 2OCJ, all four p53 chains and the structurally coordinated Zn^{2+} ions were retained. Crystallographic water molecules and other non-essential heteroatoms were removed, protein protonation states were assigned at pH 7.4, and PFOA and PFOS were modeled in their deprotonated anionic forms. Binding-pocket detection and blind docking were performed using CB-Dock2 with default parameters (Liu et al. 2022). For each protein–ligand pair, the pose with the lowest Vina score was selected for subsequent analysis. Protein–ligand interactions were analyzed using the Protein–Ligand Interaction Profiler (PLIP) (Salentin et al. 2015), and the complexes were visualized in PyMOL.

2.6. Molecular dynamics and binding free-energy analysis

The docked PFOA–c-Jun, PFOS–c-Jun, PFOA–p53, and PFOS–p53 complexes were used as starting structures for 100-ns molecular dynamics simulations in GROMACS version 2023.2 (Abraham et al. 2015). Proteins were parameterized using the AMBER99SB-ILDN force field and solvated with the transferable intermolecular potential with three points (TIP3P) water model. Austin Model 1–bond charge correction (AM1-BCC) partial charges were assigned to PFOA and PFOS, and ligand topologies were generated using Sobtop version 1.0 (dev5) (Jakalian et al. 2002; Lu 2024). Each system was placed in a periodic water box and neutralized with Na^+ or Cl^- ions, followed by energy minimization, 2 ns of equilibration in the canonical (NVT) ensemble and 2 ns of equilibration in the

isothermal–isobaric (NPT) ensemble. Production simulations were performed at 300 K and 1 bar using a 2-fs time step, particle mesh Ewald electrostatics, 1.0-nm Coulomb and van der Waals cutoffs, the V-rescale thermostat, the Parrinello–Rahman barostat, and Linear Constraint Solver (LINCS) constraints.

Trajectories were evaluated using root mean square deviation (RMSD), root mean square fluctuation (RMSF), radius of gyration (Rg), solvent-accessible surface area (SASA), protein–ligand hydrogen bonds, and conformational free-energy landscapes based on RMSD and Rg. Mean structural metrics were calculated over the 80–100 ns interval, whereas conformational free-energy landscapes were constructed from the complete 0–100 ns trajectories. Molecular mechanics Poisson–Boltzmann surface area (MM-PBSA) calculations were performed over the 80–100 ns interval using gmx_MMPBSA version 1.6.4, including energy-component and per-residue decomposition analyses (Valdés-Tresanco et al. 2021). For the p53 systems, whole-complex RMSD and Rg were calculated across all four retained core-domain chains.

2.7. Chemicals and cell culture

Potassium perfluorooctanoate was used as the PFOA source (CAS No. 2395-00-8; purity ≥98.0%; Cat. No. P768632; Aladdin, China), whereas PFOS was supplied as potassium perfluorooctanesulfonate (CAS No. 2795-39-3; purity ≥92.0%; Cat. No. WA37121; Guangdong Wengjiang Chemical Reagent Co., Ltd., China). PFOA and PFOS were prepared as 200 mM stock solutions in dimethyl sulfoxide (DMSO).

Primary human umbilical vein endothelial cells (HUVECs; Cat. No. CCP-H001; Shanghai Kerui Cell Biotechnology Co., Ltd., China) were cultured in endothelial cell medium (ECM; Cat. No. CMP-1001) at 37 °C in a humidified atmosphere containing 5% CO_2. Cells at passages 3–6 were used for experiments at 80%–90% confluence. All PFOA/PFOS exposure experiments were performed in ECM containing 0.5% (v/v) fetal bovine serum (FBS).

2.8. Cell viability and exposure conditions

HUVEC viability was evaluated using the Cell Counting Kit-8 (CCK-8) assay. Cells were seeded in 96-well plates at 5×10^3 cells/well and exposed for 24 h to PFOA, PFOS, or an equimolar PFOA/PFOS mixture at concentrations of 0, 6.25, 12.5, 25, 50, 100, 150, or 200 μM for each

compound in a final volume of 100 μL/well. For the combined-exposure series, the indicated concentration referred to the concentration of each compound. Cell-free wells containing medium and CCK-8 reagent served as blanks. After exposure, 10 μL of CCK-8 reagent (Cat. No. CK04; Dojindo, Japan) was added to each well, followed by incubation at 37 °C for 2 h. Absorbance at 450 nm was measured using an ELX-800 microplate reader. After blank subtraction, cell viability was normalized to the control group.

Based on the viability screening, subsequent experiments included four groups: Control, PFOA (50 μM), PFOS (50 μM), and PFOA + PFOS (50 μM + 50 μM). The final DMSO concentration was adjusted to 0.05% (v/v) in all groups. The selected nominal concentration was used to assess short-term in vitro responses and was not intended to replicate typical human serum exposure. Reverse transcription quantitative PCR (RT-qPCR), Western blotting, and scratch assays were performed after 24 h of exposure, whereas vascular-like network formation was assessed after 12 h.

2.9. Cell migration and vascular-like network formation

For the scratch assay, HUVECs were grown to 90%–100% confluence and scratched using a sterile 200-μL pipette tip. Cells were washed twice with phosphate-buffered saline (PBS) to remove detached cells and debris and then subjected to the indicated treatments in ECM containing 0.5% FBS. The same fields were imaged at 0 and 24 h, and the migration rate was calculated from changes in scratch area using ImageJ.

For the vascular-like network formation assay, 20 μL of Matrigel basement membrane matrix (Cat. No. 356234; Corning, USA) was placed in the center of each well of a 24-well plate and polymerized at 37 °C for 30 min. HUVECs were then seeded at 1.5×10^5 cells/well and subjected to the indicated treatments. After 12 h, network structures were imaged, and the number of junctions and total segment length were quantified using the Angiogenesis Analyzer plugin in ImageJ (Carpentier et al. 2020).

2.10. RNA extraction and RT-qPCR

After 24 h of exposure, total RNA was extracted using TRIpure Reagent (Cat. No. RN01; Aidlab, China), and complementary DNA (cDNA) was synthesized using the ReverTra Ace qPCR RT Kit (Cat. No. FSQ-101; Toyobo, Japan). Quantitative PCR was performed on a LightCycler 96 system (Roche Diagnostics GmbH, Germany) using 2× UltraSYBR Mixture (Cat. No. CW0957M; CWBIO,

China) in a total reaction volume of 10 μL. Glyceraldehyde-3-phosphate dehydrogenase (*GAPDH*) was used as the reference gene, and the relative expression levels of *IL6*, *IL1A*, and *CXCL8* were calculated using the 2−ΔΔCt method (Livak and Schmittgen 2001). Primer sequences are provided in Supplementary Table S1.

2.11. Western blotting

After 24 h of exposure, HUVECs were lysed in radioimmunoprecipitation assay (RIPA) buffer containing protease and phosphatase inhibitors. Protein concentrations were determined using the bicinchoninic acid (BCA) assay. Equal amounts of protein were separated by sodium dodecyl sulfate–polyacrylamide gel electrophoresis (SDS-PAGE) and transferred onto 0.45-μm polyvinylidene difluoride (PVDF) membranes. Membranes were blocked with 5% bovine serum albumin (BSA) for 1 h at room temperature and incubated overnight at 4 °C with primary antibodies against GAPDH, p53, c-Jun, phospho-c-Jun (Ser63), nuclear factor-κB (NF-κB) p65, phospho-p65 (Ser536), endothelial nitric oxide synthase (eNOS), phospho-eNOS (Ser1177), vascular cell adhesion molecule 1 (VCAM-1) and intercellular adhesion molecule 1 (ICAM-1). Horseradish peroxidase (HRP)-conjugated secondary antibodies and enhanced chemiluminescence were used for signal detection with a GeneGnome XRQ imaging system. Band intensities were quantified using Fiji. VCAM-1, ICAM-1, and p53 were normalized to GAPDH, whereas phosphorylated proteins were normalized to their corresponding total proteins. Antibody information is provided in Supplementary Table S2.

2.12. Statistical analysis

Statistical analyses of the cellular experiments were performed using GraphPad Prism version 9.5.1. Data are presented as the mean ± standard deviation (SD) from three independent biological replicates ($n = 3$). Comparisons among the four groups were performed using one-way analysis of variance (ANOVA), followed by Dunnett's multiple-comparisons test comparing each exposure group with the control group. $P < 0.05$ was considered statistically significant. No formal mixture-interaction model was applied to the combined-exposure group. Statistical annotations in figures are reported as follows: ns, $P \geq 0.05$; *$P < 0.05$; **$P < 0.01$; ***$P < 0.001$.

3. Results

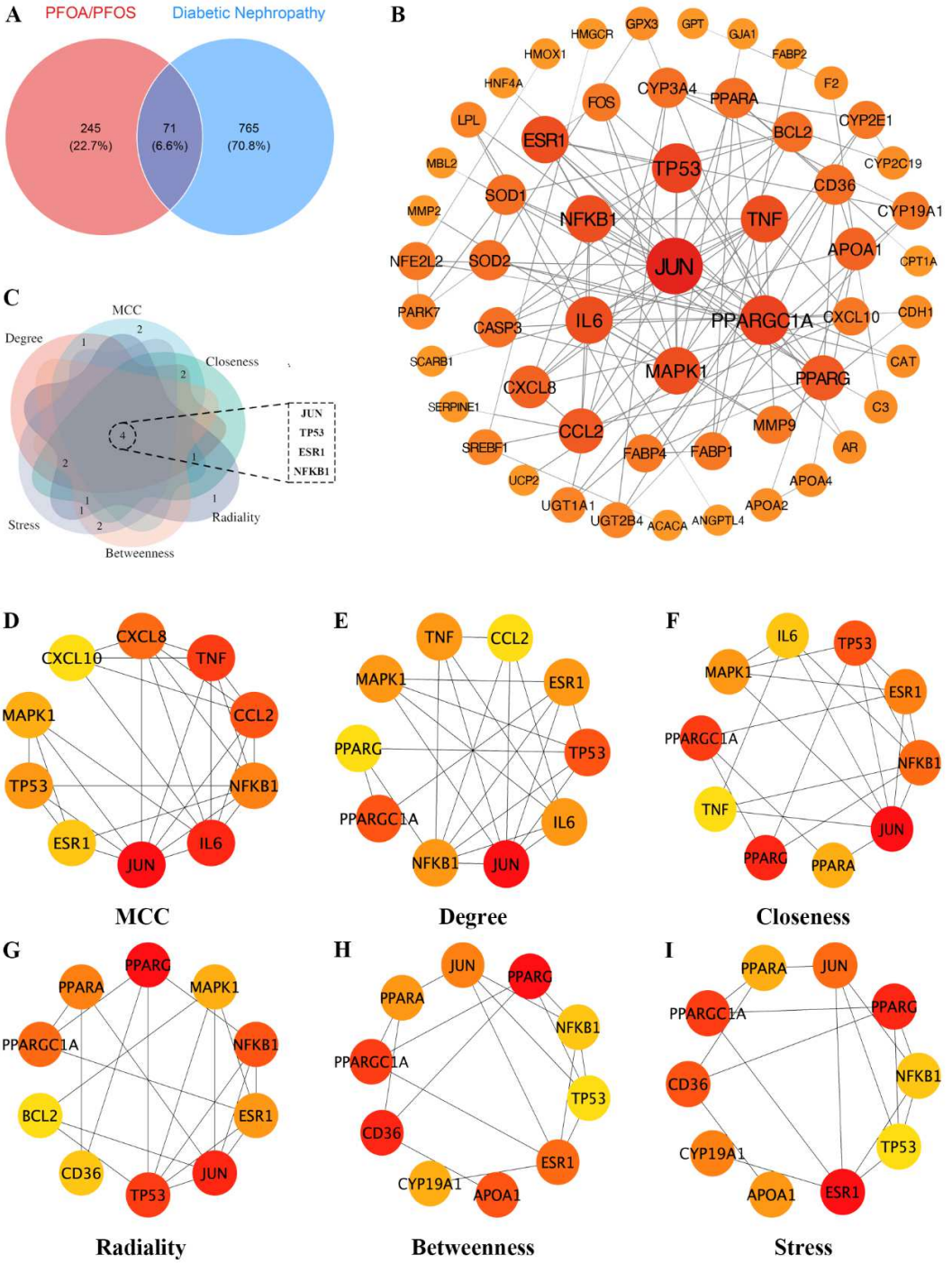
3.1. Cross-disease hub-gene analysis

After identifier standardization and deduplication, 749 PFOA-associated targets and 599 PFOS-associated targets were obtained, of which 316 were shared by both compounds. These 316 shared targets were separately intersected with gene sets associated with six diabetic complications, yielding 71 overlapping genes for diabetic nephropathy, 64 for diabetic retinopathy, 89 for diabetic neuropathy, 89 for diabetic foot ulcer, 137 for diabetic vascular dysfunction, and 93 for diabetic cardiomyopathy (Supplementary Fig. S1A). Diabetic vascular dysfunction showed the largest number of overlapping genes, whereas diabetic retinopathy showed the smallest, indicating different degrees of overlap between the shared PFOA/PFOS target set and the gene sets of individual diabetic complications.

Protein–protein interaction networks were then constructed from the complication-specific overlapping genes. Each network contained multiple highly connected inflammation-, stress-, and metabolism-related nodes, with *JUN* and *TP53* appearing as prominent nodes across all six disease networks; *TNF*, *IL6*, *MAPK1*, *MAPK3*, *NFKB1*, and *ESR1* also recurred across multiple networks (Figs. 1–6).

The six disease networks were further ranked in parallel using the MCC, Degree, Closeness, Radiality, Betweenness, and Stress algorithms implemented in cytoHubba. In the diabetic nephropathy, diabetic retinopathy, and diabetic neuropathy networks, *JUN*, *TP53*, *ESR1*, and *NFKB1* were simultaneously ranked among the top 10 by all six algorithms. The six-algorithm consensus genes were *JUN*, *TP53*, and *RELA* in diabetic foot ulcer; *JUN* and *TP53* in diabetic vascular dysfunction; and *JUN*, *TP53*, and *ESR1* in diabetic cardiomyopathy (Figs. 1–6).

Comparison of the recurrence frequency of these six-algorithm consensus genes across the six disease networks showed that *JUN* and *TP53* met the consensus criterion in 6/6 networks and were the only genes retained across all six diabetic complications (Supplementary Fig. S1B). *ESR1* occurred in 4/6 networks, *NFKB1* in 3/6 networks, and *RELA* in 1/6 networks. Thus, *JUN* and *TP53* showed the highest cross-disease and cross-algorithm consistency and were prioritized as candidate molecular nodes for subsequent structural analyses and cellular experimental evaluation.



254

255 Fig. 1. PFOA/PFOS-related hub genes associated with diabetic nephropathy. (A) Intersection of shared
256 PFOA/PFOS targets and diabetic nephropathy-associated genes. (B) PPI network constructed from the 71
257 common targets; isolated nodes were removed before visualization. (C) Overlap of the top 10 genes ranked
258 by six cytoHubba algorithms; JUN, TP53, ESR1, and NFKB1 were shared across all six algorithms. (D–I)
259 Rankings by MCC, Degree, Closeness, Radiality, Betweenness, and Stress, respectively.

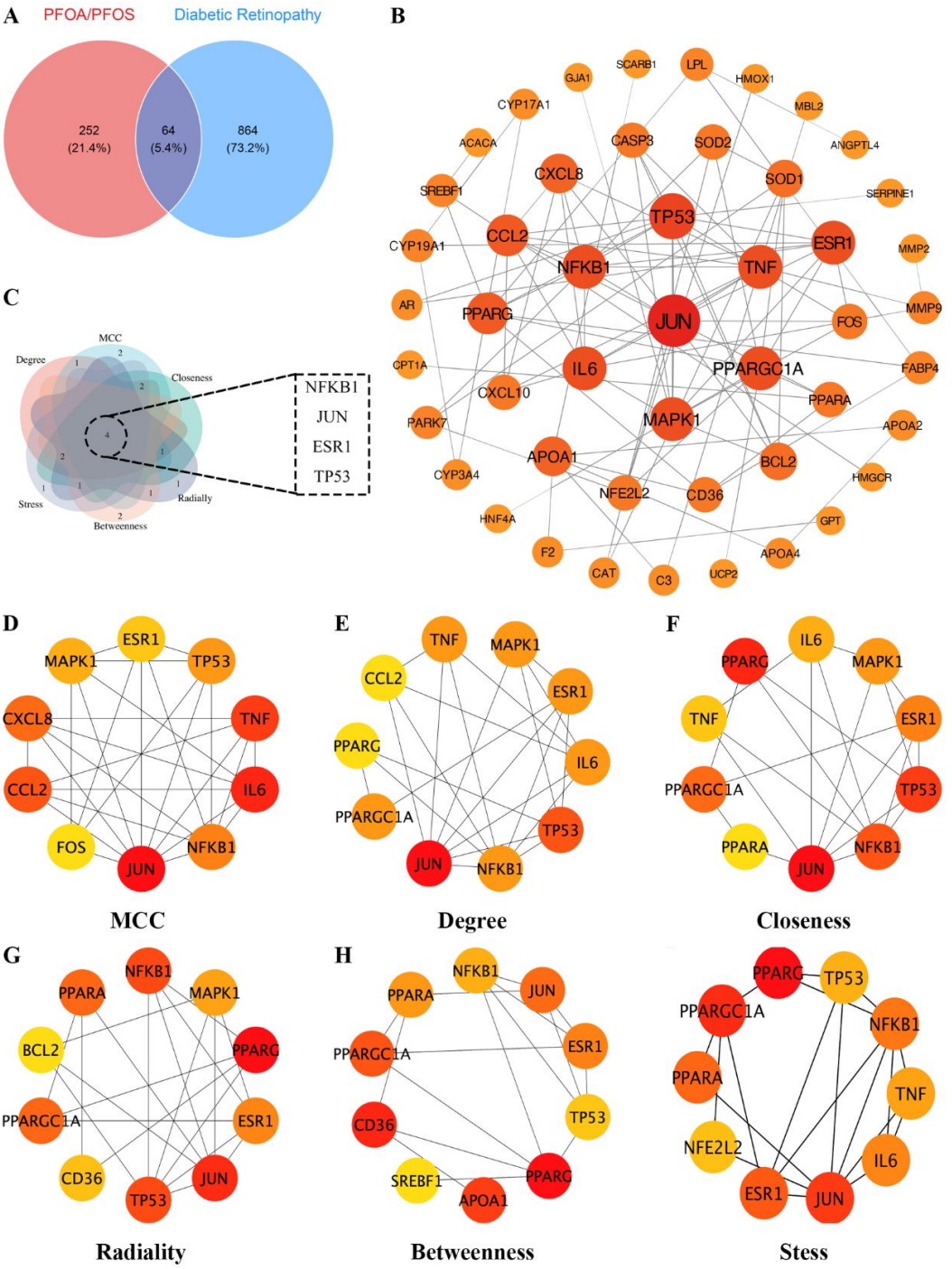


Fig. 2. PFOA/PFOS-related hub genes associated with diabetic retinopathy. (A) Intersection of shared PFOA/PFOS targets and diabetic retinopathy-associated genes. (B) PPI network constructed from the 64 common targets; isolated nodes were removed before visualization. (C) Overlap of the top 10 genes ranked by six cytoHubba algorithms; JUN, TP53, NFKB1, and ESR1 were shared across all six algorithms. (D–I) Rankings by MCC, Degree, Closeness, Radiality, Betweenness, and Stress, respectively.

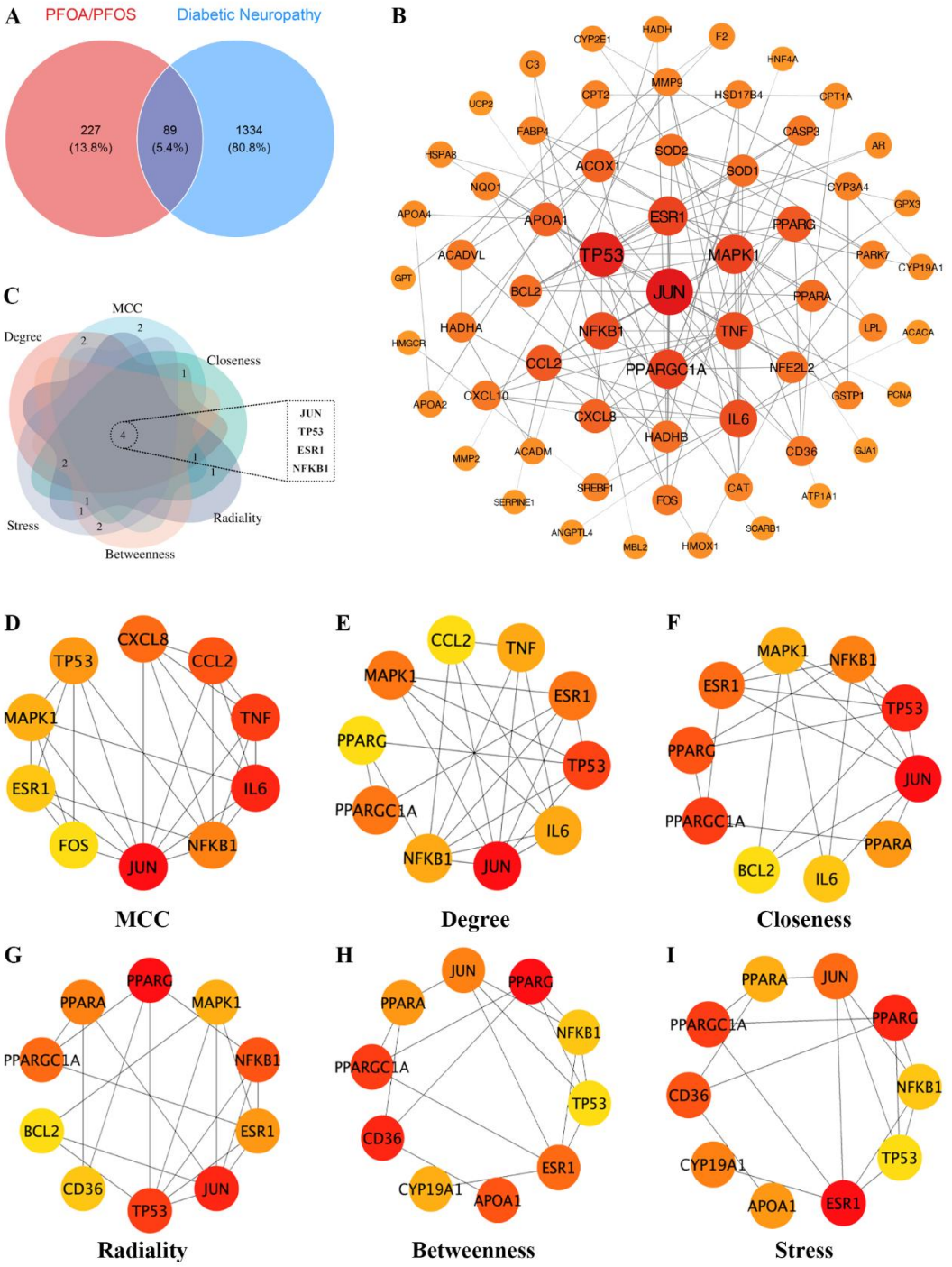


Fig. 3. PFOA/PFOS-related hub genes associated with diabetic neuropathy. (A) Intersection of shared PFOA/PFOS targets and diabetic neuropathy-associated genes. (B) PPI network constructed from the 89 common targets; isolated nodes were removed before visualization. (C) Overlap of the top 10 genes ranked by six cytoHubba algorithms; JUN, TP53, ESR1, and NFKB1 were shared across all six algorithms. (D–I) Rankings by MCC, Degree, Closeness, Radiality, Betweenness, and Stress, respectively.

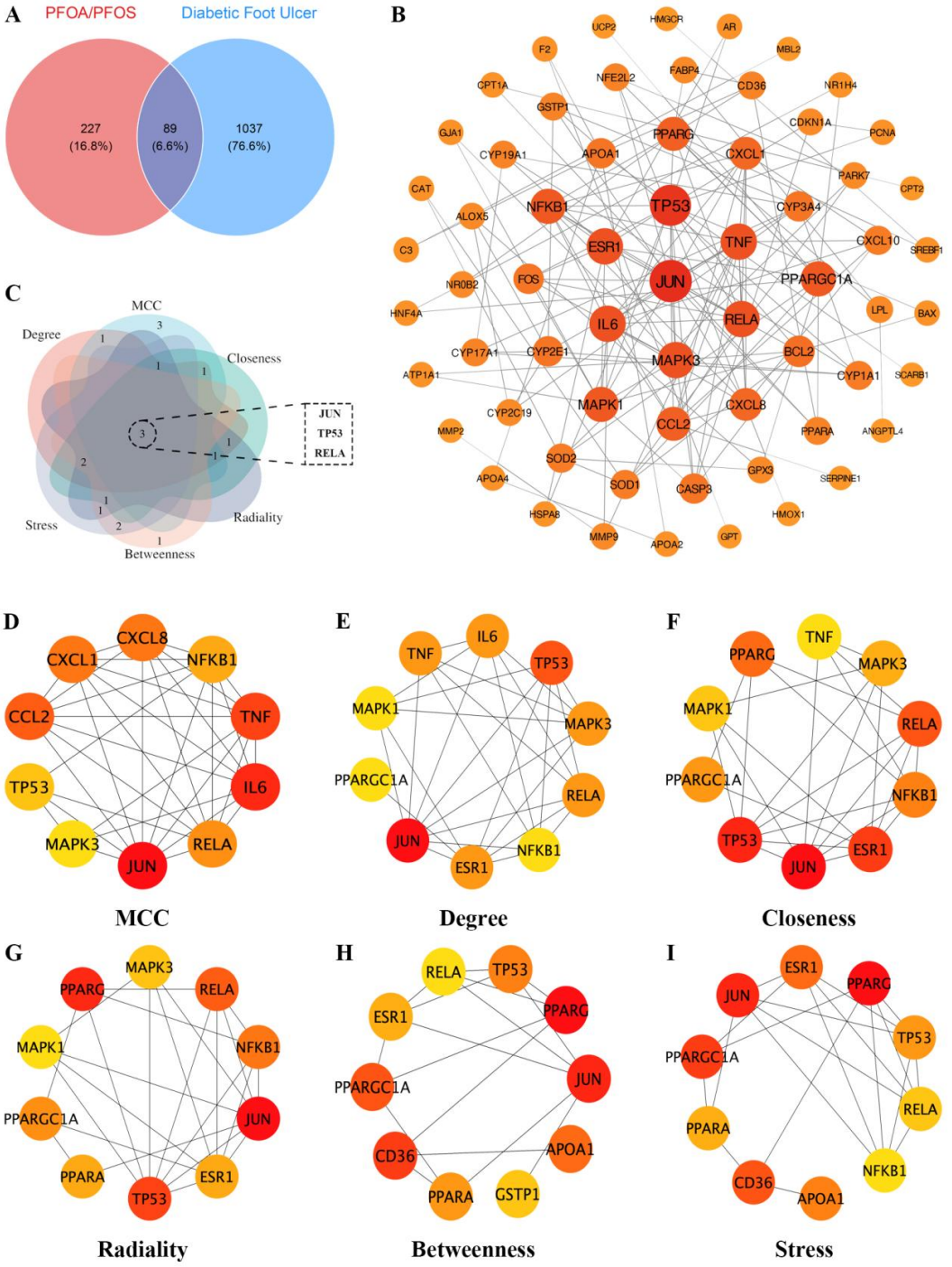


Fig. 4. PFOA/PFOS-related hub genes associated with diabetic foot ulcer. (A) Intersection of shared PFOA/PFOS targets and diabetic foot ulcer-associated genes. (B) PPI network constructed from the 89 common targets; isolated nodes were removed before visualization. (C) Overlap of the top 10 genes ranked by six cytoHubba algorithms; JUN, TP53, and RELA were shared across all six algorithms. (D–I) Rankings by MCC, Degree, Closeness, Radiality, Betweenness, and Stress, respectively.

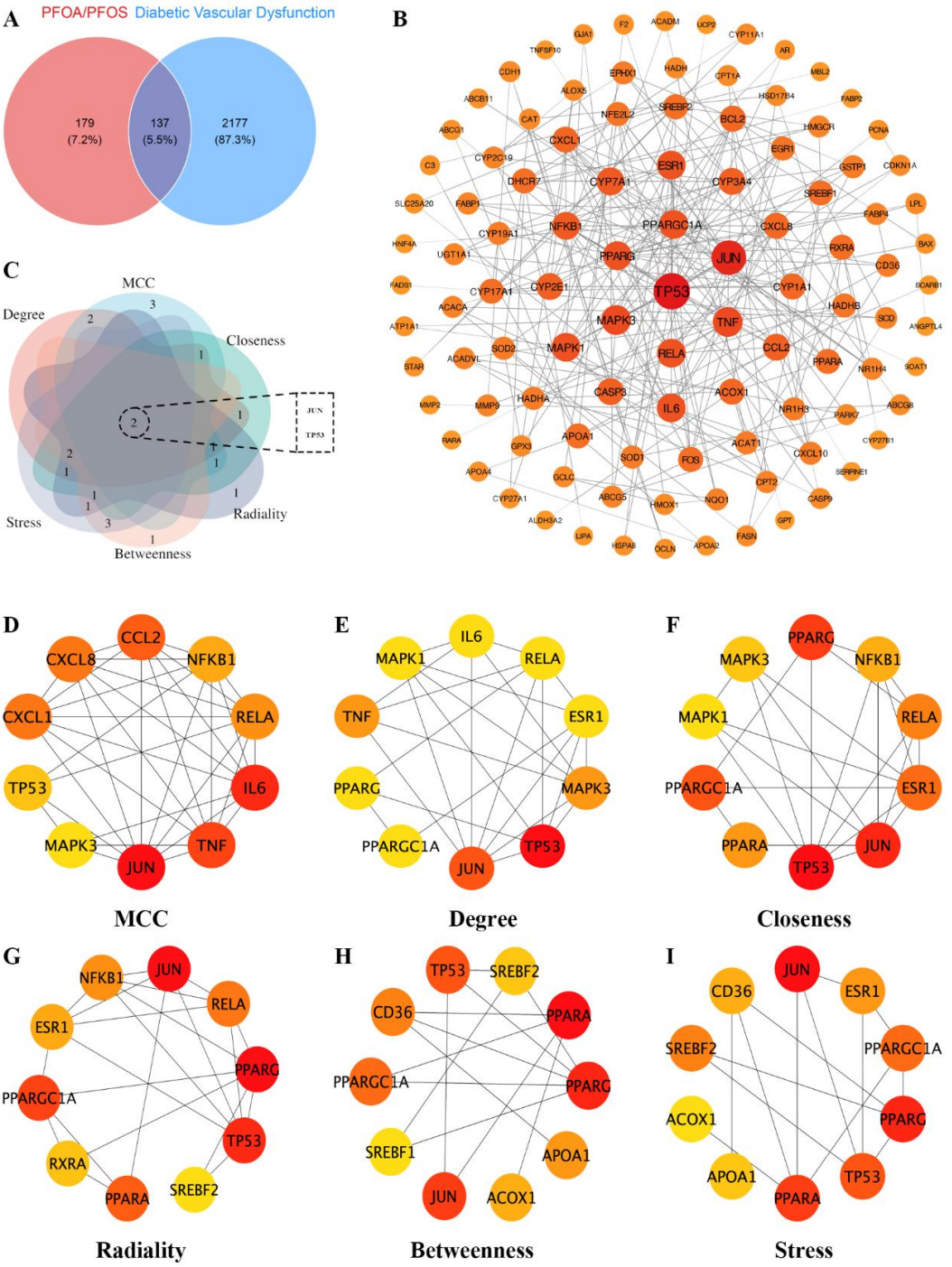
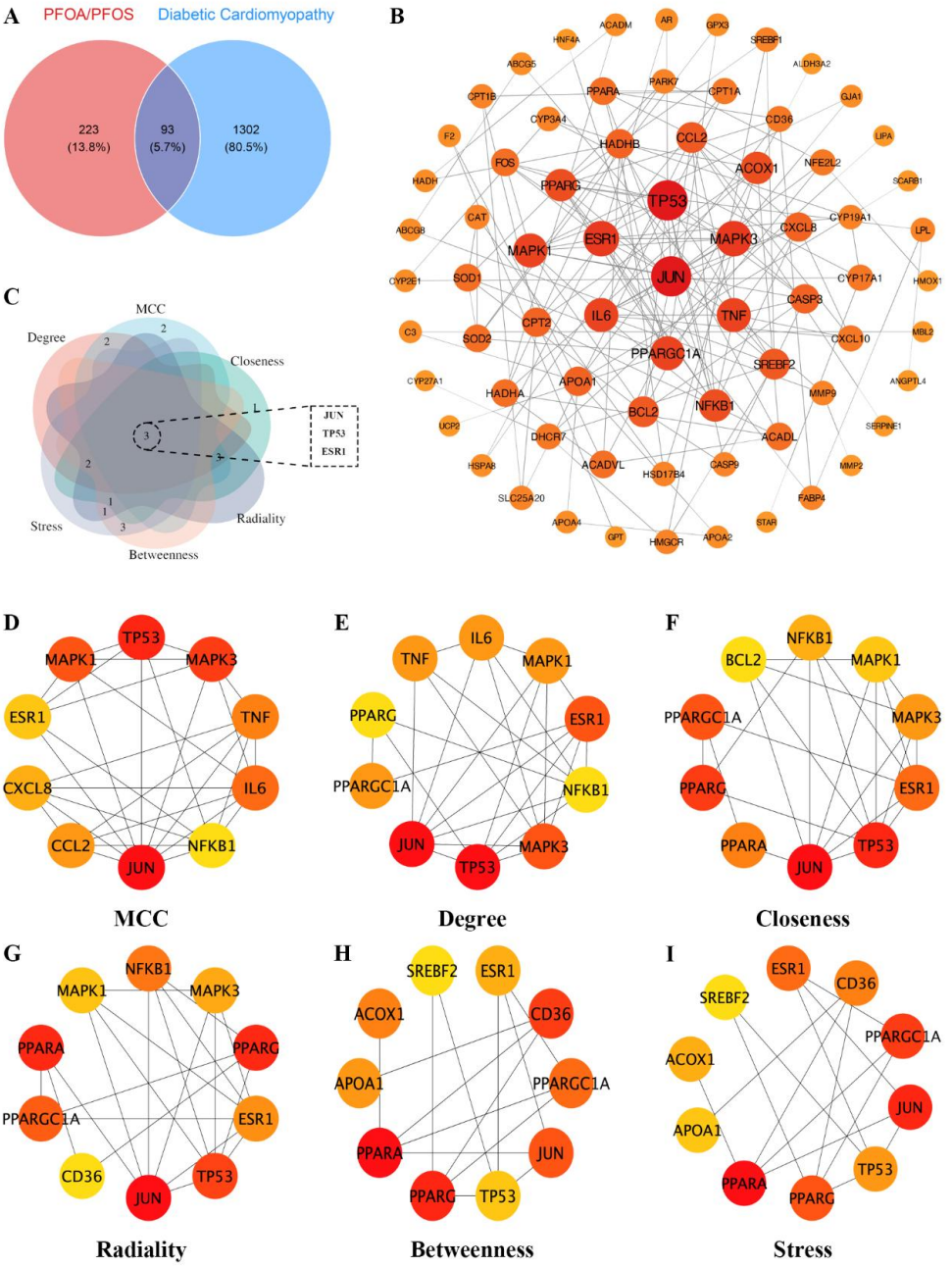


Fig. 5. PFOA/PFOS-related hub genes associated with diabetic vascular dysfunction. (A) Intersection of shared PFOA/PFOS targets and diabetic vascular dysfunction-associated genes. (B) PPI network constructed from the 137 common targets; isolated nodes were removed before visualization. (C) Overlap of the top 10 genes ranked by six cytoHubba algorithms; JUN and TP53 were shared across all six algorithms. (D–I) Rankings by MCC, Degree, Closeness, Radiality, Betweenness, and Stress, respectively.



284

285 Fig. 6. PFOA/PFOS-related hub genes associated with diabetic cardiomyopathy. (A) Intersection of shared
286 PFOA/PFOS targets and diabetic cardiomyopathy-associated genes. (B) PPI network constructed from the
287 93 common targets; isolated nodes were removed before visualization. (C) Overlap of the top 10 genes
288 ranked by six cytoHubba algorithms; JUN, TP53, and ESR1 were shared across all six algorithms. (D–I)
289 Rankings by MCC, Degree, Closeness, Radiality, Betweenness, and Stress, respectively.

3.2. Functional enrichment across disease networks

Although the enrichment profiles differed among the six diabetic complications, several biological themes recurred across the six networks, mainly involving lipid metabolism, inflammation, and oxidative stress-related processes.

GO analysis showed that lipid-related terms were broadly enriched across all six networks, including lipid homeostasis, fatty acid and steroid metabolism, and lipid transport and localization. Specifically, the diabetic nephropathy network was enriched for lipid homeostasis, lipid transport, and steroid metabolism. The diabetic retinopathy network additionally showed triglyceride and acylglycerol metabolism, together with lipid-particle-related cellular-component terms. Terms related to fatty acid metabolism and degradation, responses to xenobiotics, and antioxidant activity were more prominent in diabetic neuropathy and diabetic foot ulcer. Diabetic vascular dysfunction was mainly associated with cholesterol and fatty acid metabolism and lipid transport, whereas diabetic cardiomyopathy showed enrichment of terms related to the peroxisomal membrane and fatty acid catabolism. Terms related to oxidative stress and responses to reactive oxygen species recurred in the diabetic nephropathy, retinopathy, neuropathy, and foot ulcer networks, whereas molecular-function terms including nuclear receptor activity, ligand-activated transcription factor activity, and transcription coregulator binding were enriched across multiple networks (Supplementary Figs. S2, S4, S6, S8, S10, and S12).

KEGG analysis further showed that Lipid and atherosclerosis, PPAR signaling pathway, AGE–RAGE signaling pathway in diabetic complications, and IL-17 signaling pathway were recurrently enriched across all six disease networks. Cholesterol metabolism was also represented in all six networks. In addition, TNF signaling pathway was enriched in the diabetic retinopathy and diabetic foot ulcer networks; Fluid shear stress and atherosclerosis was more prominent in the diabetic retinopathy and diabetic neuropathy networks; Bile secretion and Fat digestion and absorption were observed in the diabetic nephropathy, diabetic vascular dysfunction, and diabetic cardiomyopathy networks; and Fatty acid metabolism and Fatty acid degradation were particularly evident in the diabetic neuropathy and diabetic cardiomyopathy networks (Supplementary Figs. S3, S5, S7, S9, S11, and S13).

Cross-disease comparison showed that diabetic vascular dysfunction had the largest overlap with the shared PFOA/PFOS target set, comprising 137 genes, with enrichment mainly involving lipid transport, PPAR signaling, and lipid- and atherosclerosis-related pathways. In contrast, diabetic cardiomyopathy showed greater representation of lipid catabolism and peroxisome-related processes, whereas responses to xenobiotics and antioxidant-related processes were more prominent in diabetic neuropathy and diabetic foot ulcer. Diabetic retinopathy additionally showed enrichment of pathways related to fluid shear stress and atherosclerosis. Overall, the six disease networks exhibited recurrent metabolic, inflammatory, and stress-related enrichment patterns.

3.3. Molecular docking of PFOA/PFOS with c-Jun and p53

To evaluate the potential structural compatibility of PFOA and PFOS with c-Jun and p53, molecular docking was performed using PDB IDs 1JNM and 2OCJ, respectively (Fig. 7).

Vina scoring yielded docking scores of −5.0, −5.1, −4.1, and −4.3 kcal/mol for PFOA–c-Jun, PFOS–c-Jun, PFOA–p53, and PFOS–p53, respectively. PFOS showed slightly lower scores than PFOA in both protein systems, but the differences were only 0.1–0.2 kcal/mol, indicating broadly similar predicted docking scores for the two compounds within the corresponding protein systems.

Binding-mode analysis showed that PFOA formed predicted interactions with LYS273, ARG272, and SER269 in c-Jun, including a salt bridge between its carboxylate group and ARG272 together with a predicted halogen-bond contact. PFOS formed predicted interactions with LYS288, ARG272, ARG276, and ARG279, including salt-bridge and halogen-bond contacts. In the p53 system, PFOA formed predicted interactions with ARG248, ARG273, GLY105, and GLN104, whereas PFOS formed hydrogen-bond, halogen-bond, and electrostatic contacts with ARG282, ARG283, GLU286, and GLU287.

Overall, PFOA and PFOS both formed predicted binding poses with c-Jun and p53, while their Vina scores were broadly similar within the corresponding protein systems. The docking results provide structural clues regarding potential binding modes and served as starting conformations for the subsequent molecular dynamics simulations.

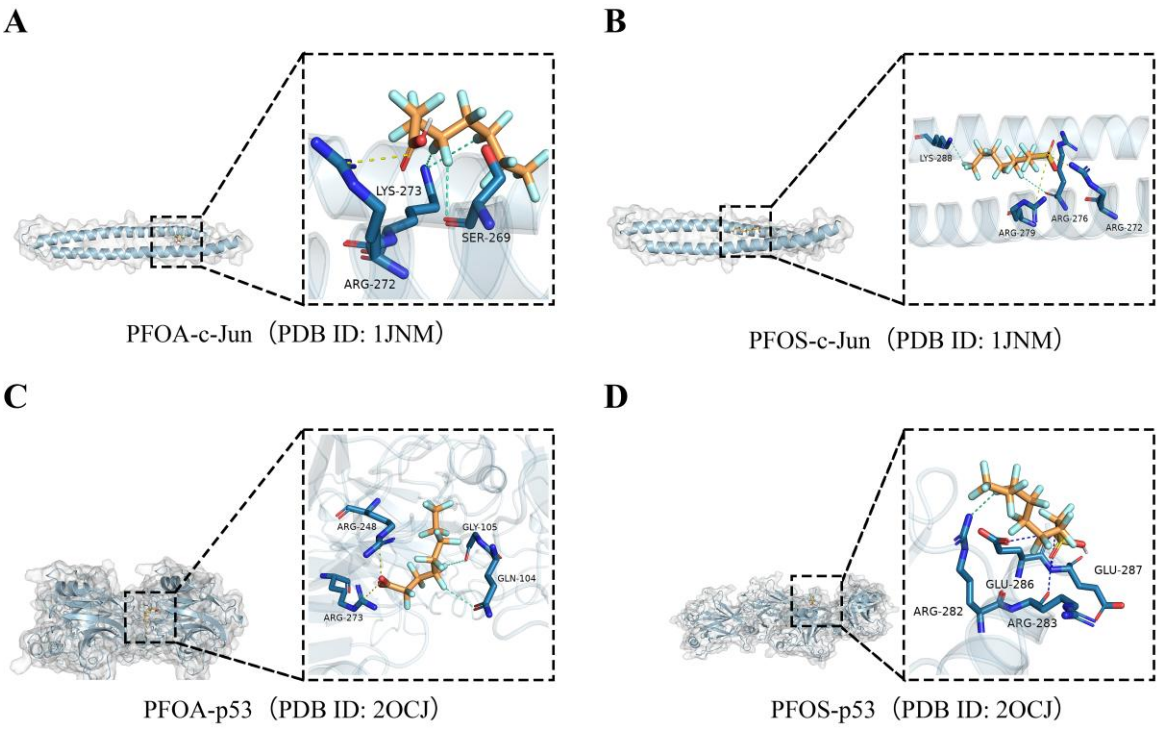


Fig. 7. Molecular docking of PFOA and PFOS with c-Jun and p53. (A) PFOA–c-Jun; (B) PFOS–c-Jun; (C) PFOA–p53; and (D) PFOS–p53. The left panels show the overall predicted binding poses, and the right panels show the major protein–ligand interactions.

3.4. Molecular dynamics of PFOA/PFOS–protein complexes

To further compare the dynamic behavior of the four predicted complexes, 100-ns molecular dynamics simulations were performed for PFOA–c-Jun, PFOS–c-Jun, PFOA–p53, and PFOS–p53. Mean structural parameters and MM-PBSA binding free-energy estimates were calculated over the 80–100 ns trajectory interval, whereas conformational free-energy landscapes were constructed from the complete 0–100 ns trajectories using RMSD and Rg as reaction coordinates (Fig. 8).

In the c-Jun systems, the two complexes showed broadly similar dynamic behavior. Over the 80–100 ns interval, the mean RMSD values of PFOA–c-Jun and PFOS–c-Jun were 1.33 and 1.31 nm, respectively, and their RMSF profiles were also similar. The mean Rg of PFOS–c-Jun was 2.67 nm, compared with 2.85 nm for PFOA–c-Jun, while the mean numbers of protein–ligand hydrogen bonds were 3.00 and 1.55, respectively. The conformational free-energy landscape of PFOS–c-Jun showed a visually more concentrated major low-energy region. MM-PBSA analysis yielded binding free-energy estimates of −10.88 kcal/mol for PFOA–c-Jun and −13.06 kcal/mol for PFOS–c-Jun. Per-residue energy decomposition showed relatively favorable contributions from ARG272, ARG276, and

LYS273 in the PFOA–c-Jun system, whereas ARG279, ARG276, LYS283, LYS285, and LYS288 contributed favorably in the PFOS–c-Jun system.

More pronounced differences were observed between the two p53 systems. Over the 80–100 ns interval, the mean whole-complex RMSD values were 2.65 nm for PFOA–p53 and 1.45 nm for PFOS–p53. The Rg of the PFOA–p53 system increased from approximately 3.84 to 4.43 nm, whereas that of the PFOS–p53 system decreased from approximately 3.82 to 3.44 nm. Mean SASA values were similar between the two complexes, at 392.74 nm^2 for PFOA–p53 and 393.08 nm^2 for PFOS–p53. The mean number of protein–ligand hydrogen bonds was higher for PFOA–p53 than for PFOS–p53 (2.47 vs. 1.60). The conformational free-energy landscape of PFOS–p53 showed a visually more concentrated major low-energy region. MM-PBSA analysis yielded binding free-energy estimates of −3.81 kcal/mol for PFOA–p53 and −9.72 kcal/mol for PFOS–p53. Per-residue energy decomposition identified ARG248 as a major favorable contributor in the PFOA–p53 system, whereas ARG282 and ARG283 contributed favorably in the PFOS–p53 system; the mean contributions of GLU286 and GLU287 were positive.

Overall, the two c-Jun systems displayed broadly similar dynamic behavior, whereas the p53 systems showed more pronounced compound-dependent differences, with PFOS–p53 exhibiting lower whole-complex root mean square deviation (RMSD) and Rg values and a more favorable MM-PBSA binding free-energy estimate (Supplementary Fig. S14).

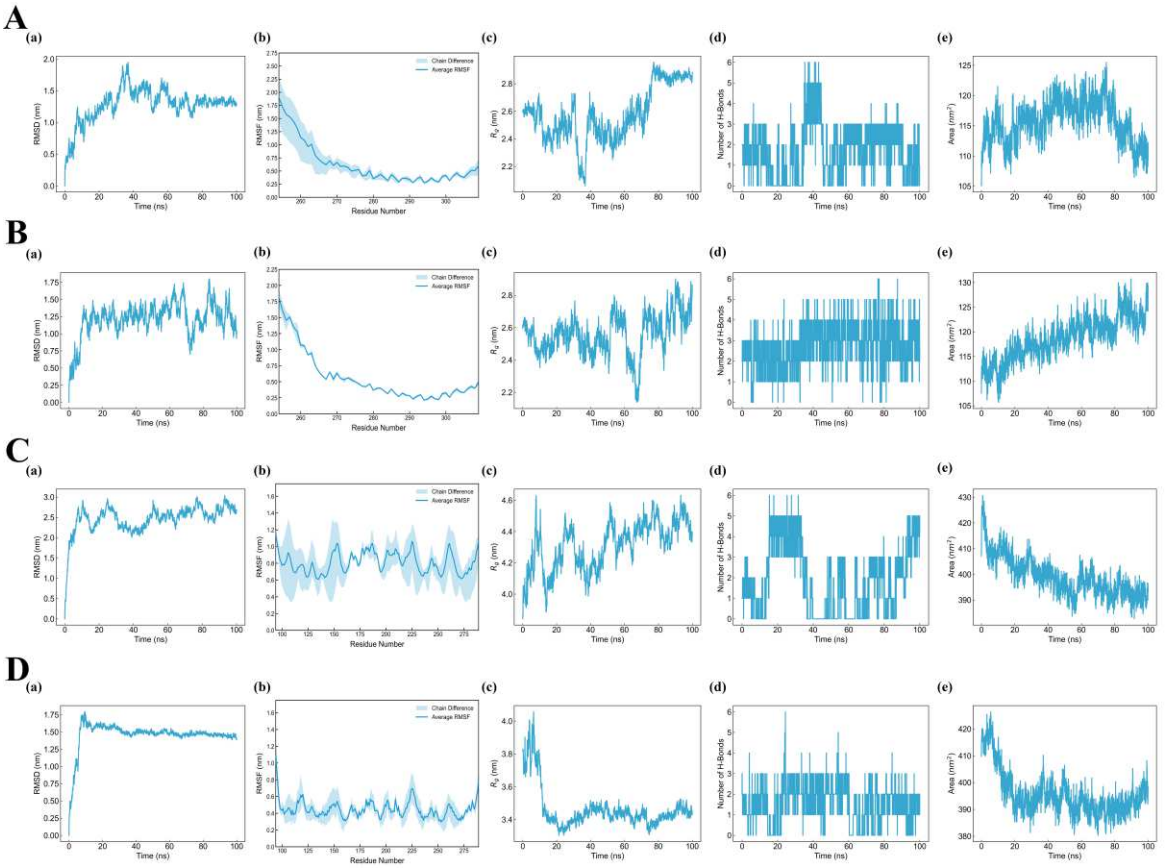


Fig. 8. Molecular dynamics analyses of PFOA and PFOS complexes with c-Jun and p53. (A) PFOA–c-Jun; (B) PFOS–c-Jun; (C) PFOA–p53; and (D) PFOS–p53. Subpanels show (a) whole-complex root mean square deviation (RMSD), (b) residue-level root mean square fluctuation (RMSF), (c) radius of gyration (Rg), (d) number of protein–ligand hydrogen bonds, and (e) solvent-accessible surface area (SASA). Trajectories cover 0–100 ns; mean values reported in the text were calculated over 80–100 ns. For the p53 systems, whole-complex RMSD and Rg values include all four core-domain chains retained from PDB ID 2OCJ.

3.5. Cell viability and concentration selection

To determine the exposure concentrations for subsequent HUVEC experiments, cell viability was first assessed after 24 h of exposure to PFOA, PFOS, or equimolar combined exposure. Cell viability was normalized to the untreated control group (0 μM), which was set to 100%. As the exposure concentration increased, cell viability decreased across all three exposure series, with larger reductions in the PFOS and mixture groups than in the PFOA group at higher concentrations (Supplementary Fig. S15).

At 50 μM, cell viability was 87.98 ± 2.11% in the PFOA group and 83.05 ± 2.43% in the PFOS group, whereas the combined-exposure group (50 μM PFOA + 50 μM PFOS) showed a viability of 79.45 ± 2.56%. At 50 μM, cell viability ranged from 79.45% to 87.98% across the exposure groups. Therefore, 50 μM PFOA, 50 μM PFOS, and combined exposure to 50 μM PFOA + 50 μM PFOS were used for subsequent molecular and functional experiments.

3.6. Molecular responses to PFOA/PFOS exposure

Western blot analysis showed that PFOA, PFOS, and combined exposure produced distinct patterns of protein expression and phosphorylation (Fig. 9A, B). Compared with the control group, PFOS exposure significantly increased ICAM-1 (1.784 ± 0.069, $P < 0.01$), p53 (1.393 ± 0.093, $P < 0.001$), p-p65/p65 (3.438 ± 0.841, $P < 0.001$), and p-c-Jun/c-Jun (1.430 ± 0.159, $P < 0.01$). Combined exposure significantly increased ICAM-1 (1.703 ± 0.211, $P < 0.05$), VCAM-1 (1.994 ± 0.227, $P < 0.05$), p53 (1.251 ± 0.048, $P < 0.05$), p-p65/p65 (2.624 ± 0.340, $P < 0.01$), and p-c-Jun/c-Jun (1.314 ± 0.069, $P < 0.01$). PFOA exposure alone significantly increased only p-p65/p65 (2.380 ± 0.346, $P < 0.05$). No significant differences in the p-eNOS/eNOS ratio were observed between any exposure group and the control group ($P > 0.05$).

PFOS exposure was accompanied by increases in both the p-c-Jun/c-Jun ratio and p53 protein levels, consistent with the prioritization of *JUN* and *TP53* in the cross-disease network analysis.

RT-qPCR analysis showed that PFOS exposure significantly increased *IL6* and *IL1A* mRNA expression (both $P < 0.001$; Fig. 9C), whereas the changes observed in the PFOA and combined-exposure groups did not reach statistical significance compared with the control ($P \geq 0.05$). The greatest increases were observed in the PFOS group, with relative expression levels of 53.422 ± 7.491 for *IL6* and 43.530 ± 5.437 for *IL1A*. The corresponding values were 8.142 ± 1.072 and 4.068 ± 0.397 in the PFOA group and 8.194 ± 0.433 and 3.543 ± 0.197 in the combined-exposure group. *CXCL8* showed a different transcriptional response pattern: PFOS exposure significantly increased *CXCL8* expression (2.527 ± 0.236, $P < 0.001$), whereas PFOA (0.335 ± 0.030, $P < 0.001$) and combined exposure (0.520 ± 0.035, $P < 0.01$) significantly decreased its expression.

Overall, PFOA, PFOS, and combined exposure produced distinct molecular response patterns. PFOS was accompanied by broader inflammation- and stress-related molecular changes, whereas combined exposure produced an endpoint-dependent response distinct from the PFOS-alone condition.

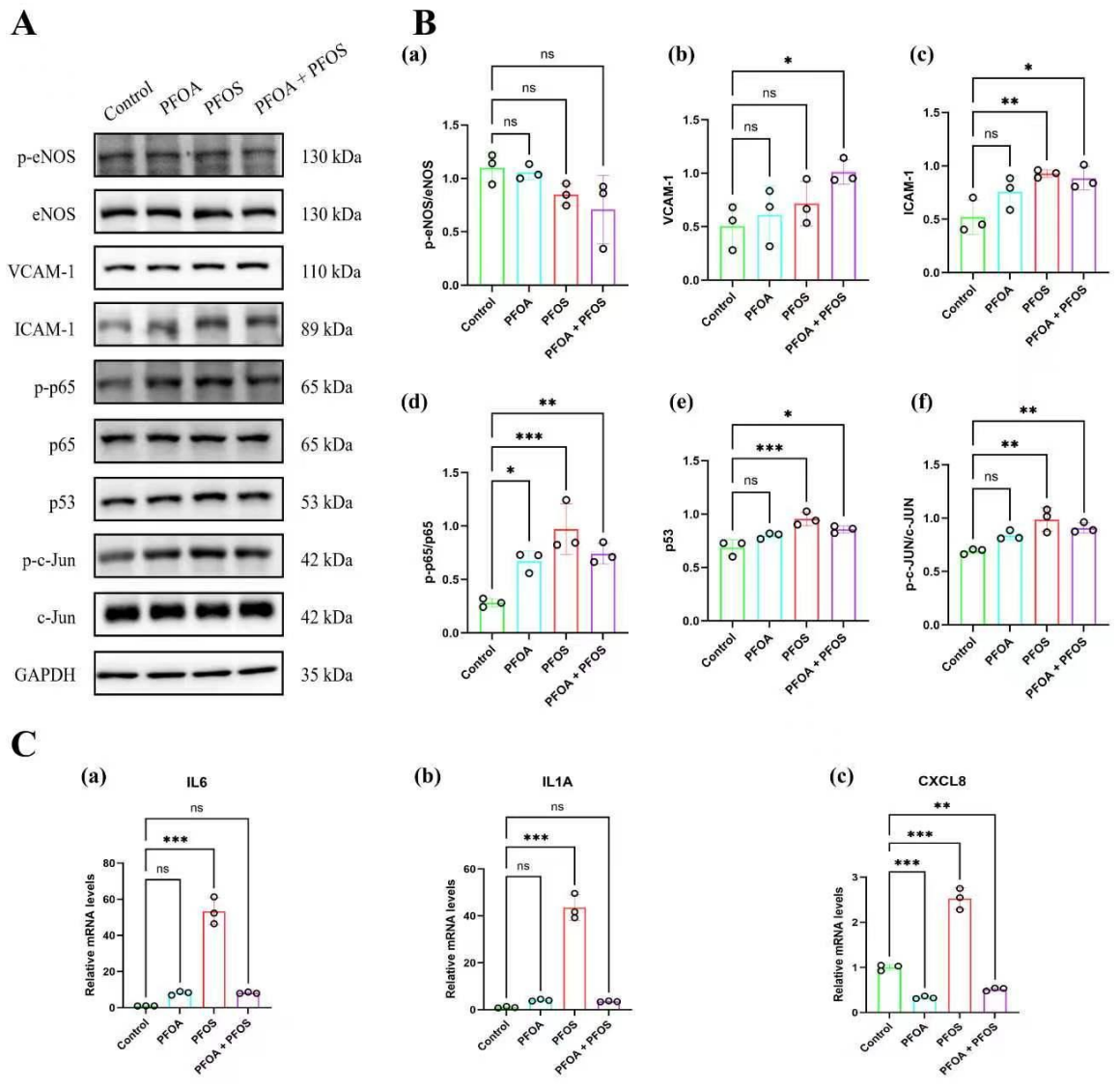


Fig. 9. Effects of PFOA, PFOS, and their combination on inflammatory, stress-related, and endothelial markers in HUVECs. (A) Representative Western blots of p-eNOS, eNOS, ICAM-1, VCAM-1, p-p65, p65, p53, p-c-Jun, and c-Jun; GAPDH served as the loading control. (B) Quantification of (a) p-eNOS/eNOS, (b) VCAM-1/GAPDH, (c) ICAM-1/GAPDH, (d) p-p65/p65, (e) p53/GAPDH, and (f) p-c-Jun/c-Jun. (C) GAPDH-normalized relative mRNA expression of (a) IL6, (b) IL1A, and (c) CXCL8. Data are presented as the mean ± SD from three independent biological replicates (n = 3). Statistical significance was assessed by one-way ANOVA followed by Dunnett's multiple-comparisons test, with each exposure group compared with the control group. ns, $P \geq 0.05$; *$P < 0.05$; **$P < 0.01$; ***$P < 0.001$.

3.7. Effects on endothelial migration and network formation

The scratch assay showed that PFOS exposure significantly reduced the 24-h migration rate of HUVECs (36.90 ± 7.66% vs. 56.45 ± 0.54% in the control group, $P < 0.05$), and combined exposure also significantly reduced migration (21.22 ± 14.32%, $P < 0.01$; Fig. 10A, C). PFOA exposure alone had no significant effect on migration rate (47.21 ± 2.49%, $P > 0.05$).

The Matrigel vascular-like network formation assay showed that all three exposure conditions significantly reduced the number of junctions (all $P < 0.01$; Fig. 10B, D(a)). The numbers of junctions in the control, PFOA, PFOS, and combined-exposure groups were 55.67 ± 3.79, 32.33 ± 10.50, 28.67 ± 6.43, and 25.00 ± 6.08, respectively. For total segment length, significant reductions were observed in the PFOS group (1937.67 ± 355.40, $P < 0.05$) and the combined-exposure group (1792.00 ± 617.98, $P < 0.05$) compared with the control group (3191.00 ± 161.90), whereas no significant difference was observed in the PFOA group (2206.67 ± 671.06, $P > 0.05$; Fig. 10D(b)).

Overall, PFOS and combined exposure reduced HUVEC migration and vascular-like network formation, whereas the functional effects of PFOA alone were comparatively limited.

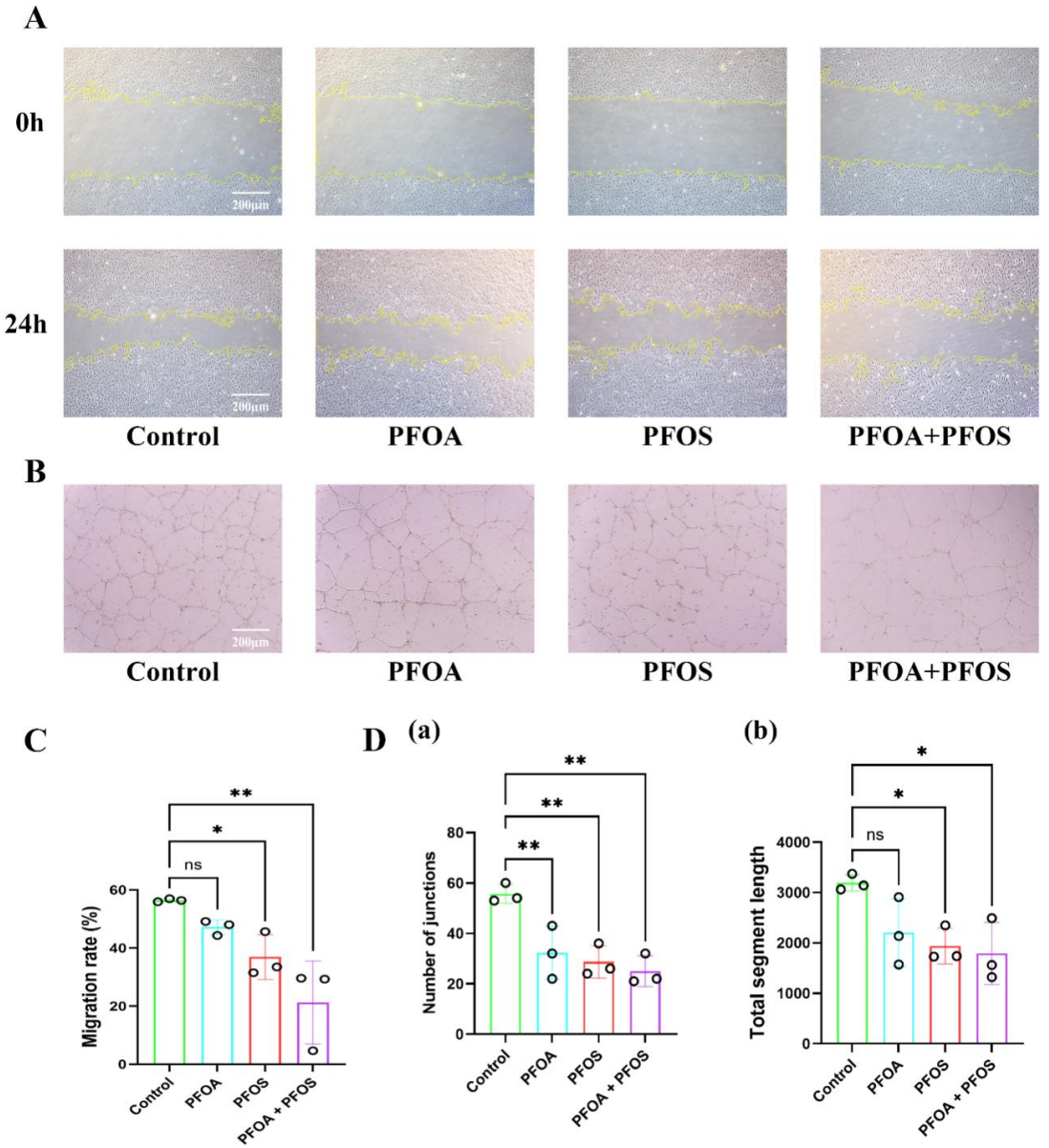


Fig. 10. Effects of PFOA, PFOS, and their combination on HUVEC migration and vascular-like network formation. (A) Representative wound-healing images at 0 and 24 h; yellow lines indicate the wound boundaries. (B) Representative images of Matrigel-based vascular-like networks. (C) Migration rate calculated from wound closure at 24 h. (D) Quantification of (a) the number of junctions and (b) total segment length. Scale bars = 200 μm. Data are presented as the mean ± SD from three independent biological replicates (n = 3). Statistical significance was assessed by one-way ANOVA followed by Dunnett's multiple-comparisons test, with each exposure group compared with the control group. ns, $P \geq 0.05$; *$P < 0.05$; **$P < 0.01$.

4. Discussion

PFOA and PFOS are persistent fluorinated chemicals with distinct anionic head groups. Their parallel comparison offers a chemical rationale for examining differences in predicted protein interactions and short-term endothelial responses. In the present study, network toxicology was used to identify candidate nodes within six diabetes-related gene sets; docking and molecular dynamics provided exploratory structural models, and HUVEC experiments measured molecular and functional effects. The diabetic-complication networks were used for biological context and not as substitutes for a diabetes model in the experiments.

The most consistent network-level finding was the recurrent appearance of *JUN* and *TP53* across six clinically distinct diabetic complications. Although diabetic nephropathy, retinopathy, neuropathy, foot ulcer, vascular dysfunction, and cardiomyopathy affect different tissues and organs, they all involve, to varying degrees, endothelial activation, redox imbalance, chronic inflammation, and disrupted metabolic regulation (Schalkwijk and Stehouwer 2005; Shi and Vanhoutte 2017). *JUN* and *TP53* ranked among the top 10 nodes by all six cytoHubba algorithms in every disease network, indicating strong cross-disease and cross-algorithm consistency. *JUN* encodes c-Jun, a core component of the activator protein-1 (AP-1) transcription factor that responds to oxidative stress, inflammatory mediators, and environmental stimuli (Morton et al. 2003), whereas *TP53* encodes p53, which participates in DNA damage responses, cell-cycle regulation, senescence, and apoptosis and has been linked to endothelial stress and vascular dysfunction (Yokoyama et al. 2019). Previous PFAS toxicology studies have likewise implicated stress- and inflammation-related pathways, including p53 and TNF-α/NF-κB signaling, in PFOA-associated cellular effects (Li et al. 2017). Thus, the recurrent identification of *JUN*/*TP53* is biologically plausible and suggests that c-Jun/p53-related stress regulation may represent a shared PFAS-associated molecular feature across diabetic-complication contexts.

Consistent with this interpretation, enrichment analysis showed recurrent involvement of lipid and atherosclerosis, PPAR signaling, AGE–RAGE signaling in diabetic complications, and IL-17 signaling across the six disease networks, together with cholesterol metabolism, fatty acid metabolism, oxidative stress, and nuclear receptor-related functions. Associations of PFOA/PFOS with disturbed

lipid homeostasis are well documented in epidemiological and mechanistic studies and involve lipid transport, nuclear receptor regulation, and multiple metabolic pathways (Fragki et al. 2021). PPAR- and lipid metabolism enrichment is thus consistent with known metabolic-disrupting features of PFAS, whereas AGE–RAGE and IL-17 signaling further connect metabolic stress with inflammatory activation. c-Jun/AP-1 participates in downstream transcriptional regulation of multiple inflammatory pathways, and p53 is closely involved in oxidative stress and cell-fate regulation. Together, these findings establish a coherent network-level link between the cross-disease hub genes and metabolic–inflammatory–stress pathways.

Structural modeling further revealed compound-dependent differences between PFOA and PFOS. Molecular docking yielded broadly similar Vina scores for the two compounds in both c-Jun and p53 systems, differing by only 0.1–0.2 kcal/mol, indicating that docking scores alone did not distinguish PFOA from PFOS. In contrast, 100-ns molecular dynamics (MD) simulations and MM-PBSA analyses showed clearer differences in the p53 systems: compared with PFOA–p53, PFOS–p53 exhibited lower whole-complex root mean square deviation (RMSD) and Rg values and a more favorable binding free-energy estimate, whereas the two c-Jun systems showed similar dynamic behavior. Previous studies have likewise reported compound-dependent differences between PFOA and PFOS—Chi et al. (2018) observed stronger PFOS binding in a serum albumin system, and Tsuda (2016) summarized differential toxicological responses across several experimental contexts—supporting the view that PFOA and PFOS should not be assumed to behave identically. Here, whole-complex RMSD and Rg were calculated across all four retained p53 chains and should be interpreted alongside MM-PBSA, hydrogen-bond, and per-residue energy-decomposition results. Because 2OCJ represents the isolated p53 core domain and a crystallographic four-chain arrangement, these whole-complex metrics cannot be interpreted as stability measures for full-length cellular p53. Importantly, these structural analyses were used for comparative hypothesis generation and do not establish direct binding of PFOA or PFOS to c-Jun or p53.

Cellular experiments were conducted in standardized HUVEC culture without added high glucose or AGEs, first to isolate endothelial responses attributable to PFOA/PFOS themselves. The Control, PFOA, PFOS, and PFOA + PFOS grouping followed comparative frameworks used in prior

individual- and combined-exposure studies (Ojo et al. 2021; Spyrou et al. 2024) and provides a basis for future evaluation under diabetes-relevant metabolic stress.

HUVEC experiments showed that PFOS exposure produced marked changes in p-c-Jun/c-Jun, p-p65/p65, p53, ICAM-1, and inflammatory transcripts including *IL6*, *IL1A*, and *CXCL8*, whereas PFOA alone altered fewer molecular endpoints. Because *JUN* and *TP53* were independently nominated by cross-disease network analysis before the cellular experiments, the subsequent c-Jun- and p53-related changes provide cross-platform consistency between network prediction and experimental observation. Prior endothelial studies support these findings: Qian et al. (2010) reported that PFOS promoted ROS generation, cytoskeletal remodeling, and increased permeability in human microvascular endothelial cells, and Liao et al. (2012) observed PFOS effects on oxidative stress, inflammatory genes, and adhesion responses in HUVECs. Together with the concurrent c-Jun/NF-κB, p53, adhesion, and inflammatory changes seen here, these findings indicate a prominent inflammatory and cellular stress response to PFOS. In contrast, p-eNOS/eNOS did not change significantly in any group, indicating no clear eNOS Ser1177 phosphorylation response under the present 24-h exposure conditions.

These molecular changes were accompanied by impaired endothelial functional phenotypes. PFOS and combined exposure significantly reduced HUVEC migration and decreased both junction number and total segment length in vascular-like network formation, whereas PFOA alone mainly reduced junction number. Forsthuber et al. (2022) similarly reported that PFOS inhibited vascular-like structure formation and reduced branching and structural length in a HUVEC/fibroblast 3D co-culture model. Although culture systems and exposure conditions differed, both studies indicate that PFOS impairs endothelial cells' ability to form vascular-like structures. These functional impairments occurred concurrently with c-Jun/NF-κB, p53, adhesion, and inflammatory changes, providing a consistent direction of effects across network prioritization, molecular responses, and functional phenotypes. PFOS also affected a broader range of endpoints than PFOA, paralleling the clearer compound-dependent differences in p53 structural simulations, although a causal link remains to be established experimentally.

Combined exposure produced an endpoint-dependent response rather than a simple amplification of the PFOS-alone effect. It significantly affected multiple inflammation/stress-related proteins and functional endpoints, but *IL6* and *IL1A* increases were similar in magnitude to PFOA alone and substantially smaller than PFOS alone, whereas *CXCL8* changed in the opposite direction to PFOS alone. Prior mixture studies indicate that combined effects vary with dose, mixture composition, and biological model: Conley et al. (2022) found in pregnant rats that most shared endpoints were reasonably predicted by dose-addition models despite endpoint-specific differences, and Gray et al. (2024) showed in Japanese quail that mixture interpretation requires an explicit dose-addition framework. Because the present combined condition was 50 μM PFOA + 50 μM PFOS—with a total nominal PFAS concentration higher than either single-compound condition—and equal-total-dose controls and a systematic mixture model were not used, these data are best interpreted as a descriptive combined-exposure response profile, not evidence of additivity, synergy, or antagonism.

The 50 μM working concentration was selected from viability screening to observe molecular and functional responses under short-term in vitro conditions and is not intended to reproduce typical human internal exposure. Human serum PFOA/PFOS concentrations are generally in the ng/mL range—reported in Japanese monitoring (Nakayama et al. 2005) and even in the highly exposed Veneto population in Italy (Batzella et al. 2024)—far below the present in vitro concentration. This study should therefore be regarded as an acute in vitro hazard-identification and candidate-mechanism prioritization model and not directly extrapolated to real-world exposure; future work should use lower concentrations, longer durations, and concentration–response designs relevant to environmental exposure.

Several limitations should be considered. Network analysis was influenced by database coverage, annotation quality, and computational prediction. Cellular experiments used only one short-term working concentration and one combined-exposure ratio, and therefore could not fully characterize concentration–response relationships or mixture interactions. Although standardized HUVEC conditions helped isolate PFAS-specific endothelial effects, HUVECs are a large-vessel model and no diabetes-related metabolic stressor was superimposed, so the model cannot reproduce organ-specific diabetic microvascular environments. Residual viability differences among groups may also have

contributed to migration and network-formation effects. In addition, lipid- and PPAR-related enrichment pathways were not directly validated, and direct binding and causal roles of c-Jun/p53 in endothelial impairment remain to be established through biophysical binding assays, pathway perturbation, or genetic manipulation.

Future studies should examine concentration–response relationships under environmentally relevant low-dose, long-term conditions and determine whether high glucose, AGEs, or organ-specific endothelial models modify PFAS-associated endothelial effects in diabetic contexts. Direct binding assays such as surface plasmon resonance (SPR) and microscale thermophoresis (MST), together with *JUN*/*TP53* gain- and loss-of-function studies, could further define the role of c-Jun/p53 in PFAS-associated endothelial dysfunction. Equal-total-dose designs across multiple mixture ratios and concentrations will also be needed to systematically evaluate PFOA/PFOS mixture-interaction patterns. In summary, the convergence of cross-disease network analysis, structural modeling, and HUVEC molecular and functional responses nominates *JUN* and *TP53* as shared, compound-sensitive candidate nodes linking PFOA/PFOS exposure to endothelial effects across diabetic-complication contexts—providing a prioritized, hypothesis-generating framework for future mechanistic and exposure-relevant validation.

5. Conclusions

At the tested nominal concentrations and short exposure times, PFOA, PFOS and their mixture produced distinct inflammation- and stress-associated responses in HUVECs. PFOS affected more of the measured molecular endpoints, whereas PFOS and the mixture reduced migration and vascular-like network formation. *JUN* and *TP53* were consistently prioritized across six diabetic-complication-associated networks, but these computational associations and the observed protein changes do not establish causal target involvement or direct PFOA/PFOS binding. The modeled chemical-dependent differences warrant further structural and biophysical investigation, and the present high-concentration responses cannot be directly extrapolated to typical environmental exposure.

Declarations

Ethics approval and consent to participate

Not applicable. This study used commercially sourced human umbilical vein endothelial cells and did not directly recruit human participants or collect human biological samples.

Consent for publication

Not applicable.

Availability of data and materials

The data supporting the findings of this study are available from the corresponding author upon reasonable request.

Competing interests

The authors declare that they have no known competing financial interests or personal relationships that could have appeared to influence the work reported in this paper.

Funding

This work was supported by the Anhui Provincial Health Research Project (Grant No. 2024Aa40016).

Authors' contributions

Honghui Liu: Writing – original draft, Conceptualization, Methodology, Investigation, Formal analysis, Data curation, Visualization. Chenyan Wang: Writing – original draft, Methodology, Investigation, Formal analysis, Data curation. Dong Chen: Writing – original draft, Methodology, Investigation, Formal analysis, Data curation. Qiqi Dong: Writing – review & editing, Validation, Resources, Supervision. Yan Wang: Writing – review & editing, Validation, Resources, Supervision. Chao Lu: Writing – review & editing, Conceptualization, Supervision, Resources, Project administration.

Acknowledgements

Not applicable.

Supplementary material

Supplementary material includes Supplementary Tables S1–S2 and Supplementary Figs. S1–S15.

References

Abraham MJ, Murtola T, Schulz R, Páll S, Smith JC, Hess B, Lindahl E (2015) GROMACS: High performance molecular simulations through multi-level parallelism from laptops to supercomputers. SoftwareX 1–2:19–25. https://doi.org/10.1016/j.softx.2015.06.001

Batzella E, Rosato I, Pitter G, Da Re F, Russo F, Canova C, Fletcher T (2024) Determinants of PFOA serum half-life after end of exposure: A longitudinal study on highly exposed subjects in the Veneto Region. Environ. Health Perspect. 132:027002. https://doi.org/10.1289/EHP13152

Buck RC, Murphy PM, Pabon MP (2012) Chemistry, properties, and uses of commercial fluorinated surfactants. In: Knepper TP, Lange FT (eds) Polyfluorinated Chemicals and Transformation Products. Handbook of Environmental Chemistry, vol 17. Springer, Berlin, Heidelberg, pp 1–24. https://doi.org/10.1007/978-3-642-21872-9_1.

Carpentier G, Berndt S, Ferratge S, Rasband W, Cuendet M, Uzan G, Albanese P (2020) Angiogenesis Analyzer for ImageJ—A comparative morphometric analysis of 'Endothelial Tube Formation Assay' and 'Fibrin Bead Assay'. Sci. Rep. 10:11568. https://doi.org/10.1038/s41598-020-67289-8

Chi Q, Li Z, Huang J, Ma J, Wang X (2018) Interactions of perfluorooctanoic acid and perfluorooctanesulfonic acid with serum albumins by native mass spectrometry, fluorescence and molecular docking. Chemosphere 198:442–449. https://doi.org/10.1016/j.chemosphere.2018.01.152

Chin CH, Chen SH, Wu HH, Ho CW, Ko MT, Lin CY (2014) cytoHubba: Identifying hub objects and sub-networks from complex interactome. BMC Syst. Biol. 8 (Suppl. 4):S11. https://doi.org/10.1186/1752-0509-8-S4-S11

Conley JM, Lambright CS, Evans N, Medlock-Kakaley E, Dixon A, Hill D, McCord J, Strynar MJ, Ford J, Gray Jr. LE (2022) Cumulative maternal and neonatal effects of combined exposure to a mixture of perfluorooctanoic acid (PFOA) and perfluorooctane sulfonic acid (PFOS) during pregnancy in the Sprague–Dawley rat. Environ. Int. 170:107631. https://doi.org/10.1016/j.envint.2022.107631

De Silva AO, Armitage JM, Bruton TA, Dassuncao C, Heiger-Bernays W, Hu XC, Kärrman A, Kelly B, Ng C, Robuck A, Sun M, Webster TF, Sunderland EM (2021) PFAS exposure pathways for humans and wildlife: A synthesis of current knowledge and key gaps in understanding. Environ. Toxicol. Chem. 40:631–657. https://doi.org/10.1002/etc.4935

Forsthuber M, Widhalm R, Granitzer S, Kaiser AM, Moshammer H, Hengstschläger M, Dolznig H, Gundacker C (2022) Perfluorooctane sulfonic acid inhibits vessel formation in a human 3D co-culture angiogenesis model (NCFs/HUVECs). Environ. Pollut. 293:118543. https://doi.org/10.1016/j.envpol.2021.118543

Fragki S, Dirven H, Fletcher T, Grasl-Kraupp B, Gützkow KB, Hoogenboom R, Kersten S, Lindeman B, Louisse J, Peijnenburg A, Piersma AH, Princen HMG, Uhl M, Westerhout J, Zeilmaker MJ, Luijten M (2021) Systemic PFOS and PFOA exposure and disturbed lipid homeostasis in humans: what do we know and what not? Crit. Rev. Toxicol. 51:141–164. https://doi.org/10.1080/10408444.2021.1888073

Glüge J, Scheringer M, Cousins IT, DeWitt JC, Goldenman G, Herzke D, Lohmann R, Ng CA, Trier X, Wang Z (2020) An overview of the uses of per- and polyfluoroalkyl substances (PFAS). Environ. Sci. Process. Impacts 22:2345–2373. https://doi.org/10.1039/d0em00291g

Gray LE, Conley JM, Bursian SJ (2024) Dose addition models accurately predict the subacute effects of a mixture of perfluorooctane sulfonate and perfluorooctanoic acid on Japanese quail (Coturnix japonica) chick mortality. Environ. Toxicol. Chem. 43:97–104. https://doi.org/10.1002/etc.5758

Gui SY, Qiao JC, Xu KX, Li ZL, Chen YN, Wu KJ, Jiang ZX, Hu CY (2023) Association between per- and polyfluoroalkyl substances exposure and risk of diabetes: A systematic review and meta-analysis. J. Expo. Sci. Environ. Epidemiol. 33:40–55. https://doi.org/10.1038/s41370-022-00464-3

Jakalian A, Jack DB, Bayly CI (2002) Fast, efficient generation of high-quality atomic charges. AM1-BCC model: II. Parameterization and validation. J. Comput. Chem. 23:1623–1641. https://doi.org/10.1002/jcc.10128

Li K, Gao P, Xiang P, Zhang X, Cui X, Ma LQ (2017) Molecular mechanisms of PFOA-induced toxicity in animals and humans: Implications for health risks. Environ. Int. 99:43–54. https://doi.org/10.1016/j.envint.2016.11.014

Liao Y, Wang J, Huang QS, Fang C, Kiyama R, Shen H, Dong S (2012) Evaluation of cellular response to perfluorooctane sulfonate in human umbilical vein endothelial cells. Toxicol. In Vitro 26:421–428. https://doi.org/10.1016/j.tiv.2012.01.011

Liu Y, Yang X, Gan J, Chen S, Xiao ZX, Cao Y (2022) CB-Dock2: Improved protein–ligand blind docking by integrating cavity detection, docking and homologous template fitting. Nucleic Acids Res. 50:W159–W164. https://doi.org/10.1093/nar/gkac394

Livak KJ, Schmittgen TD (2001) Analysis of relative gene expression data using the 2^(−ΔΔCt) method. Methods 25:402–408. https://doi.org/10.1006/meth.2001.1262

675 Lu T (2024) Sobtop (version 1.0, dev5): A tool for generating force-field parameters and GROMACS topology
676 files. https://sobereva.com/soft/Sobtop/ Accessed 15 July 2026.

677 Margolis R, Sant KE (2021) Associations between exposures to perfluoroalkyl substances and diabetes,
678 hyperglycemia, or insulin resistance: A scoping review. J. Xenobiot. 11:115–129.
679 https://doi.org/10.3390/jox11030008

680 Morton S, Davis RJ, McLaren A, Cohen P (2003) A reinvestigation of the multisite phosphorylation of the
681 transcription factor c-Jun. EMBO J. 22:3876–3886. https://doi.org/10.1093/emboj/cdg388

682 Nakayama S, Harada K, Inoue K, Sasaki K, Seery B, Saito N, Koizumi A (2005) Distributions of
683 perfluorooctanoic acid (PFOA) and perfluorooctane sulfonate (PFOS) in Japan and their toxicities. Environ.
684 Sci. 12:293–313..

685 Ojo AF, Xia Q, Peng C, Ng JC (2021) Evaluation of the individual and combined toxicity of perfluoroalkyl
686 substances to human liver cells using biomarkers of oxidative stress. Chemosphere 281:130808.
687 https://doi.org/10.1016/j.chemosphere.2021.130808

688 Qi Z, Yang X, Geng Z, Zhang L, Huang Z, Shi C, Xie Q, Zhang F (2026) Health effects of PFASs on five major
689 human cancers: A network toxicology perspective on molecular pathogenesis. J. Environ. Sci. 162:307–321.
690 https://doi.org/10.1016/j.jes.2025.09.052

691 Qian Y, Ducatman A, Ward R, Leonard S, Bukowski V, Guo NL, Shi X, Vallyathan V, Castranova V (2010)
692 Perfluorooctane sulfonate (PFOS) induces reactive oxygen species (ROS) production in human
693 microvascular endothelial cells: role in endothelial permeability. J. Toxicol. Environ. Health A 73:819–836.
694 https://doi.org/10.1080/15287391003689317

695 Salentin S, Schreiber S, Haupt VJ, Adasme MF, Schroeder M (2015) PLIP: Fully automated protein–ligand
696 interaction profiler. Nucleic Acids Res. 43:W443–W447. https://doi.org/10.1093/nar/gkv315

697 Schalkwijk CG, Stehouwer CDA (2005) Vascular complications in diabetes mellitus: The role of endothelial
698 dysfunction. Clin. Sci. (Lond.) 109:143–159. https://doi.org/10.1042/CS20050025

699 Shi Y, Vanhoutte PM (2017) Macro- and microvascular endothelial dysfunction in diabetes. J. Diabetes 9:434–
700 449. https://doi.org/10.1111/1753-0407.12521

701 Spyrou A, Vlastos D, Antonopoulou M (2024) Evidence on the genotoxic and ecotoxic effects of PFOA, PFOS
702 and their mixture on human lymphocytes and bacteria. Environ. Res. 248:118298.
703 https://doi.org/10.1016/j.envres.2024.118298

Sunderland EM, Hu XC, Dassuncao C, Tokranov AK, Wagner CC, Allen JG (2019) A review of the pathways of human exposure to poly- and perfluoroalkyl substances (PFASs) and present understanding of health effects. J. Expo. Sci. Environ. Epidemiol. 29:131–147. https://doi.org/10.1038/s41370-018-0094-1

Szklarczyk D, Kirsch R, Koutrouli M, Nastou K, Mehryary F, Hachilif R, Gable AL, Fang T, Doncheva NT, Pyysalo S, Bork P, Jensen LJ, von Mering C (2023) The STRING database in 2023: Protein–protein association networks and functional enrichment analyses for any sequenced genome of interest. Nucleic Acids Res. 51:D638–D646. https://doi.org/10.1093/nar/gkac1000

Tsuda S (2016) Differential toxicity between perfluorooctane sulfonate (PFOS) and perfluorooctanoic acid (PFOA). J. Toxicol. Sci. 41:SP27–SP36. https://doi.org/10.2131/jts.41.SP27

Valdés-Tresanco MS, Valdés-Tresanco ME, Valiente PA, Moreno E (2021) gmx_MMPBSA: A new tool to perform end-state free energy calculations with GROMACS. J. Chem. Theory Comput. 17:6281–6291. https://doi.org/10.1021/acs.jctc.1c00645

Yokoyama M, Shimizu I, Nagasawa A, Yoshida Y, Katsuumi G, Wakasugi T, Hayashi Y, Ikegami R, Suda M, Ota Y, Okada S, Fruttiger M, Kobayashi Y, Tsuchida M, Kubota Y, Minamino T (2019) p53 plays a crucial role in endothelial dysfunction associated with hyperglycemia and ischemia. J. Mol. Cell. Cardiol. 129:105–117. https://doi.org/10.1016/j.yjmcc.2019.02.010

Zhou Y, Zhou B, Pache L, Chang M, Hadj Khodabakhshi A, Tanaseichuk O, Benner C, Chanda SK (2019) Metascape provides a biologist-oriented resource for the analysis of systems-level datasets. Nat. Commun. 10:1523. https://doi.org/10.1038/s41467-019-09234-6

Supplementary Files

This is a list of supplementary files associated with this preprint. Click to download.

- Supplementarymaterial.docx